

Article

Thermal Performance Analysis of Gradient Porosity Aluminium Foam Heat Sink for Air-Cooling Battery Thermal Management System

Peizhuo Wang, Dongchen Qin *, Tingting Wang and Jiangyi Chen

School of Mechanical and Power Engineering, Zhengzhou University, Zhengzhou 450001, China; pzwang2020@163.com (P.W.); wangtingting@zzu.edu.cn (T.W.); cji1974@zzu.edu.cn (J.C.)

* Correspondence: dcqin@zzu.edu.cn

Abstract: The three dimensional thermal model of a forced air-cooling battery thermal management system (BTMS) using aluminium foam heat sink (AFHS) is established, and the effects of porosity, pore density, and mass flow rate on the thermal and flow performance are discussed numerically from the aspects of pressure drop and temperature control effectiveness. The results reveal that an AFHS can markedly reduce the battery temperature compared with the BTMS without AFHS, but it also causes huge pressure loss and increases the temperature difference between the upstream and downstream of the battery. Reducing the porosity of aluminium foam reduces the battery's average temperature, but increases the temperature difference. The increase of pore density leads to the increase of pressure drop, but has little effect on the battery temperature. Based on this, a study of the gradient porosity of the AFHS is carried out, and the thermal and flow performance are compared with the homogeneous AFHS. The results show that the AFHS with porosity-increasing gradient pattern (PIGP) in the direction perpendicular to flow reduces the pressure loss and improves flow performance. The AFHS with a porosity-decreasing gradient pattern (PDGP) in the flow direction has no obvious effect on the flow characteristics, but it can reduce the temperature difference of the battery. The direction of gradient porosity can be selected according to need. In addition, due to the energy absorption characteristics of aluminium foam, AFHS can improve the crashworthiness of the battery pack. Therefore, AFHS has great potential in air-cooled BTM.

Keywords: battery thermal management system; air-cooling; aluminium foam heat sink; gradient porosity



Citation: Wang, P.; Qin, D.; Wang, T.; Chen, J. Thermal Performance Analysis of Gradient Porosity Aluminium Foam Heat Sink for Air-Cooling Battery Thermal Management System. *Appl. Sci.* **2022**, *12*, 4628. <https://doi.org/10.3390/app12094628>

Academic Editor: Dong-Won Kim

Received: 3 April 2022

Accepted: 2 May 2022

Published: 4 May 2022

Publisher's Note: MDPI stays neutral with regard to jurisdictional claims in published maps and institutional affiliations.



Copyright: © 2022 by the authors. Licensee MDPI, Basel, Switzerland. This article is an open access article distributed under the terms and conditions of the Creative Commons Attribution (CC BY) license (<https://creativecommons.org/licenses/by/4.0/>).

1. Introduction

Traditional fuel vehicles consume a lot of oil resources, and the exhaust gas emitted by the vehicles will deteriorate air quality, be detrimental to human health, and lead to the greenhouse effect. Currently, the energy policy and development models have changed, and many countries are vigorously developing electric vehicles to curb global warming and reduce greenhouse gas emissions. Among the many kinds of electric vehicle (EV) energy storage technologies, the lithium-ion battery (LIB) stands out because of its high output power, long service life, and high output voltage [1–3]. Although LIB has many advantages, it is very sensitive to temperature, the performance of LIB will decline when the temperature is below 0 °C or above 45 °C. If the heat generated by LIB accumulates in the battery pack and cannot be eliminated in time, it will cause rising temperatures, resulting in problems such as a fast-aging speed, few cycles, and short service life of the LIB [4–6]. In serious cases, it is prone to local overheating, liquid leakage, and even thermal runaway [7–9]. Therefore, BTMS must be used for temperature control [10,11]. The acceptable operating temperature range of LIB is –20 °C to 60 °C, while the most suitable operating temperature range is 20 °C to 40 °C, and the battery temperature difference is

kept below 5 °C [12]. The common cooling methods of BTMS include air-cooling, liquid-cooling, phase change material (PCM) cooling, heat pipe cooling, and the combination of the above systems. Liquid-cooling has high cooling efficiency, but its structure is complex and heavy, and coolant leakage may cause serious consequences [13–16]. PCM cooling has a large heat capacity and does not consume electricity, but is unsuitable for use in BTMS because of the low thermal conductivity of PCM and volume expansion during phase transformation [17–19]. Due to the high thermal conductivity, the cooling effect of heat pipe cooling is good, but it has a high cost and process requirements [20–24]. Air-cooling has the advantages of light weight, low cost, and convenient maintenance, but the low thermal conductivity of air leads to a poor cooling effect. Therefore, many works are trying to improve the thermal performance of air-cooling. Chen et al. [25] tested the influence of the inlet and outlet position of air-cooling BTMS on cooling efficiency. They found that symmetrical BTMS has a higher cooling performance in the case of the inlet and outlet being located at the centre of the positive pressure air supply system. To improve the cooling efficiency, Luo et al. [26] proposed a new type of forced air-cooling BTMS, which adopts a thermal silica cooling plate-aluminate thermal plate, the experimental results show that it can effectively improve the thermal performance.

Open-cell metal foam is a new functional material with a large specific surface area, high thermal conductivity and remarkable thermal and mechanical properties. When the fluid flows through the cavity of the open foam metal, the complex three-dimensional network structure of the metal foam enhances the mixing capability for the fluid and enhances the convective heat transfer. At the same time, the mechanical and lightweight properties of foam metal can be used as energy-absorbing materials for spacecraft landing and vehicle collision. At present, it is widely used in the electronics, aerospace, and automotive industries [27–29]. Due to the excellent heat and mass transfer characteristics of open-cell foam metal, some researchers focus on metal foam-PCM composite materials for application in the BTMS [30–32]. The results of the study show that the effective thermal conductivity of PCM can be greatly improved by adding foam metal, which can further reduce the surface temperature of the battery. However, this method also has obvious shortcomings. The use of PCM leads to a decline in the mass density of the battery system, and when the heat load generated by the LIB is too high, the PCM in the metal foam can be completely melted; the cooling efficiency will be greatly reduced in this case.

Besides the above research on adding metal foam into phase change materials, some studies focus on using metal foam to improve the forced air-cooling efficiency of LIB battery thermal management. Giuliano et al. [33] designed and manufactured a more effective air-cooling battery thermal management system, which uses metal foam heat exchanger plates to circulate the ambient air through the battery pack and directly discharge heat into the environment to obtain sufficient heat dissipation capability. Mohamed et al. [34] used the numerical analysis method to investigate the influence of pin fin heat sink and porous metal foam on the cooling efficiency of Li-ion (lithium-ion) battery thermal management. Saw et al. [35] established the heat dissipation model of open-cell aluminium foam air-cooling battery module, and simulates the thermal performance and flow field of different porosity and pore density. He found that the addition of aluminium foam in the air channel significantly improved the thermal management performance of the lithium-ion battery module compared with that without aluminium foam, he believed that aluminium foam is a potential substitute for traditional folded fin or liquid cold plate. Wang et al. [36] developed the heat dissipation model of an open-cell aluminium foam air-cooling battery module, and designed the filled shape of aluminium foam to improve the temperature uniformity, which greatly reduced the temperature difference of the battery.

Although metal foam is very promising in heat dissipation applications, it is relatively new in the application of forced air-cooling BTMS. The design and optimisation of the metal foam forced air-cooling BTMS requires enormous effort. In addition, the above research on metal foam BTMS are based on homogeneous metal foam, and there is no application of gradient porosity metal foam in BTMS. Therefore, the purpose of this paper

is to investigate the thermal performance of the forced air-cooling BTMS by using gradient porosity aluminium foam. The overall process of this study is as follows: firstly, the three-dimensional thermal model of the battery module is established, and compared with the experimental data in the literature to verify the accuracy of the model. Then, seven kinds of aluminium foam with different specifications were applied to analyse and compare the effects of the porosity, and pore density on the thermal and flow performance of the battery module. Next, to further improve the thermal and flow performance, four gradient porosity schemes are proposed to investigate the influence of gradient porosity on the comprehensive performance of battery average temperature, temperature difference, and pressure loss.

2. Computational Model and Numerical Method

2.1. Model Description

The LiFePO₄ pouch battery is used in current research, the dimensions of the battery are 227 mm (long) × 160 mm (width) × 18.25 mm (thick), and the specific parameters are shown in Table 1. Figure 1 shows the CAD model of the battery module. As can be seen, the open aluminium foam core layer and two aluminium heat spreaders on either side compose an aluminium foam heat sink (AFHS), both sides of the battery are provided with the AFHS for heat dissipation, and the thickness of aluminium foam core layer and heat spreader are 6 mm and 1 mm respectively. When the battery works and generates heat, the cooling air flows through the open-cell structure of the aluminium foam core layer and transfers heat with the battery in a forced convection mode. Since the battery module is composed of a repeated arrangement of batteries, the case with a single battery module is studied in this research.

Table 1. Parameters of the 20 Ah LiFePO₄ pouch battery [35]. Reproduced with permission from [Applied energy]; published by [Elsevier], (2017).

Parameter	Value
Nominal voltage, V	3.3
Nominal capacity, Ah	19.5
Weight, kg	0.496
Specific heat capacity, J kg ⁻¹ K ⁻¹	1200
Dimensions, mm	0.227 × 0.160 × 0.008
Anode material	Graphite
Aluminium casing thickness, m	153 × 10 ⁻⁶
Cross plane thermal conductivity, W m ⁻¹ K ⁻¹	18.4/18.4/0.34

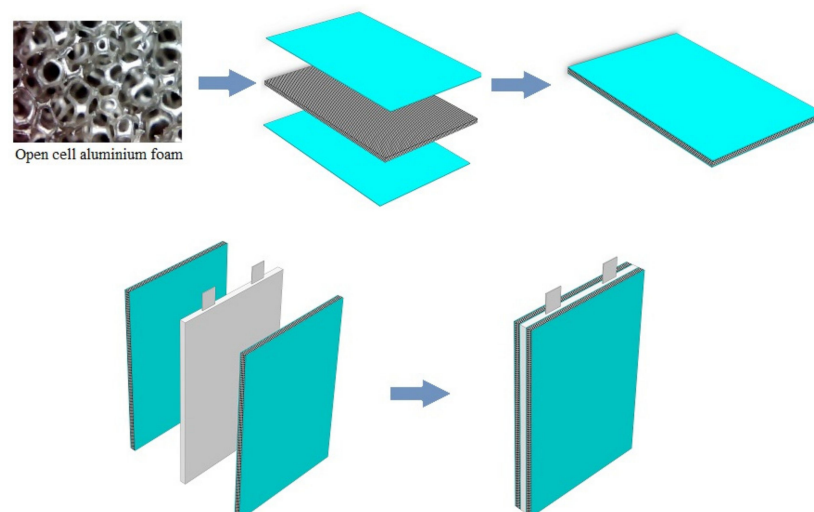


Figure 1. CAD model of battery module.

2.2. Governing Equation

The heat generated by the battery can be expressed as:

$$q = \frac{I}{V}(U_o - U) + \frac{I}{V}\left(T \frac{dU_o}{dT}\right) \tag{1}$$

in which q , V , U_o , U , and T denote heat production rate per unit volume, volume, open circuit potential, voltage, and temperature of the battery, respectively. The first term on the right side of Equation (1) represents the ohmic heat generated by the internal resistance of the battery and the irreversible heat generated by the polarisation reaction. The latter term represents reversible heat, which can be positive or negative, depending on the direction of the current and the sign of the entropy coefficient (dU_o/dT).

The energy conservation equation of the battery is as follows:

$$\frac{\partial}{\partial t}(\rho_b C_{pb} T) = \nabla \cdot (k_b \nabla T) + q \tag{2}$$

in which ρ_b indicates the density of the battery, C_{pb} indicates the heat capacity of the battery, k_b indicates the thermal conductivity of the battery.

The Forchheimer–Brinkman-extended Darcy model of the porous media and volume-averaged technique is used to describe the flow and heat transfer characteristics in aluminium foam [37]. The continuity equation can be expressed as:

$$\frac{\partial \rho_f}{\partial t} + \nabla \cdot (\rho_f \vec{v}) = 0 \tag{3}$$

where ρ_f denotes the fluid density, v denotes the average speed vector.

Conservation of momentum can be expressed as:

$$\frac{\partial}{\partial t}(\rho_f \vec{v}) + \nabla \cdot (\rho_f \vec{v} \vec{v}) = -\nabla p + \nabla \cdot \tau + \rho_f \vec{g} + S \tag{4}$$

where p represents the static pressure, S represents the source term that can be expressed as follows [38]:

$$S = -\left(\sum C_1 \mu \vec{v} + \sum C_2 \frac{1}{2} \rho |\vec{v}| \vec{v}\right) \tag{5}$$

in which μ is the fluid viscosity coefficient C_1 and C_2 are viscous resistance and inertial resistance, respectively [38], and can be expressed as:

$$C_1 = \frac{150(1 - \epsilon^2)}{d_p^2 \epsilon^3} \tag{6}$$

$$C_2 = \frac{3.5(1 - \epsilon)}{d_p \epsilon^2} \tag{7}$$

where ϵ and d_p are the porosity and pore size, respectively.

Energy conservation equation:

$$\frac{\partial}{\partial t}(\epsilon \rho_f E_f + (1 - \epsilon) \rho_s E_s) + \nabla \cdot (\vec{v} (\rho_f E_f + p)) = S_f^h + \nabla \cdot (k_{eff} \nabla T - (\sum h_i J_i) + (\tau \cdot \vec{v})) \tag{8}$$

where E_f , E_s , h , j , τ and S_f^h are the total fluid energy, total solid medium energy, sensible enthalpy, diffusion flux, stress tensor, and fluid enthalpy source term, respectively. The effective thermal conductivity k_{eff} of the aluminium foam region can be calculated as the volume average of the air thermal conductivity and the thermal conductivity of aluminium [38].

$$k_{eff} = \epsilon k_f + (1 - \epsilon) k_s \tag{9}$$

3. Numerical Simulations

3.1. Parameter Definitions

The average convective heat transfer coefficient h can be expressed as:

$$h = \frac{q}{T_w - T_{in}} \quad (10)$$

where q is heat flux applied to the bottom surface of heat sink, T_{in} is inlet air temperature and T_w is average temperature of heat transfer wall.

The average Nusselt number of the heat sink:

$$Nu = \frac{hD}{k_f} \quad (11)$$

where D denotes the equivalent diameter of heat sink, k_f denotes the thermal conductivity of the cooling medium, the equivalent diameter can be expressed as

$$D = \frac{2HW}{H + W} \quad (12)$$

where H and W represent height and width of the channel respectively.

The temperature control coefficient α and temperature uniformity coefficient β are defined to assess the comprehensive thermal performance as follows:

$$\alpha = 1 - \frac{T_{av} - T_{in}}{T_{acm} - T_{in}} \quad (13)$$

$$\beta = 1 - \frac{T_{max} - T_{min}}{\Delta T_{ac}} \quad (14)$$

where T_{av} , T_{max} , T_{min} and T_{in} are the average temperature, maximum temperature, minimum temperature and initial temperature of cooling air, respectively; T_{acm} and ΔT_{ac} are the acceptable maximum temperature and acceptable temperature difference, which are defined as 40 °C and 5 °C, respectively; T_{in} represents the initial temperature of the cooling medium, which is 26.85 °C. The closer the α is to 1, the closer the maximum temperature of the battery is to T_{in} . Similarly, the closer the β is to 1, the smaller the temperature difference of the battery is achieved, and negative β indicates that the temperature difference is greater than 5 °C.

Considering both thermal performance and flow performance, the effectiveness of improving the convective performance of the porous distribution design is further compared according to the figure of merit (FOM) [38]. FOM represents the improvement based on average heat transfer coefficients against the accompanied pumping power consumed, which means the higher the FOM, the better the comprehensive heat transfer performance of the heat sink.

$$FOM = \frac{(h_f/h_{non})}{(\Omega_f/\Omega_{non})^{\frac{1}{3}}} \quad (15)$$

where h_f and h_{non} indicate the convective heat transfer coefficient with and without aluminium foam, respectively; Ω_f and Ω_{non} indicate the required pumping power with and without aluminium foam, respectively.

$$\Omega = \frac{\dot{m}}{\rho}(p_{in} - p_{out}) \quad (16)$$

where m is the mass flow rate of cooling air, p_{in} and p_{out} are the average pressures at the inlet and outlet, respectively.

3.2. Numerical Method

Ansys-fluent is a CFD solver based on finite volume, which is used to discretize the equations introduced in the previous section. In the calculation model, the heat generation of the positive and negative plates of the battery is ignored. The cooling air of the battery module is the ideal gas. The turbulence intensity of the medium at the mass flow inlet boundary of is 5%, and the inlet temperature of cooling air is set to 26.85 °C. The pressure outlet boundary is used for the outlet, the heat transfer of the contact surface between the battery and the heat sink adopts the coupled heat transfer condition, and other walls are regarded as adiabatic conditions. The specific boundaries are shown in Figure 2. The purpose of this paper is to improve the air-cooling effect of the battery using aluminium foam. Therefore, to shorten the simulation time, the maximum heating power at 3 C discharge rate is 30 W, which is set as the average heating rate of the battery, and contact thermal resistance is ignored. The specific parameters of aluminium foams used in this work are shown in Table 2; the parameters of the heat spreader and cooling air are listed in Table 3. The energy equation and momentum equation are discretised by the second-order upwind scheme, and the coupling of pressure and velocity is solved by the SIMPLE algorithm [37]. For all simulation cases, the convergence criterion is that the residual of each governing equation is less than 1.0×10^{-6} .

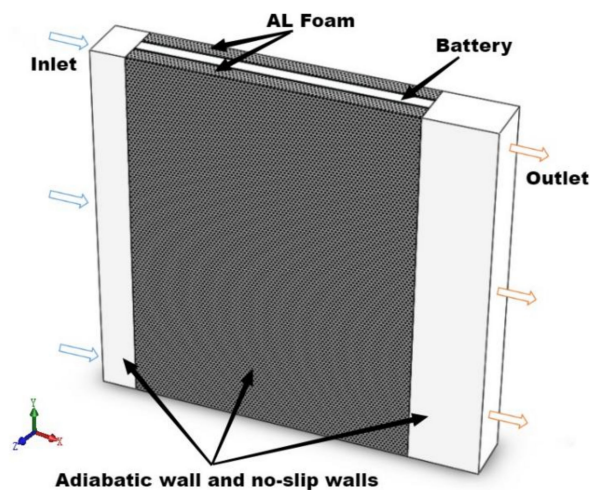


Figure 2. Boundary conditions of the battery module.

Table 2. Physical properties of aluminium foam [35]. Reproduced with permission from [Applied energy]; published by [Elsevier], (2017).

Sample	Pores Per Inch (PPI)	Ligament Diameter (mm)	Porosity
1	10	0.406	0.918
2	10	0.406	0.794
3	10	0.406	0.682
4	20	0.203	0.924
5	20	0.203	0.774
6	20	0.203	0.679
7	40	0.102	0.923

Table 3. Parameters of the heat spreader and cooling air.

	Materials	ρ (kg m ⁻³)	c_p (J kg ⁻¹ K ⁻¹)	λ (W m ⁻¹ K ⁻¹)
Base fluid	Ideal gas	1.24	1006.43	0.027
Heat spread	Aluminium	2719	871	202.4

3.3. Grid Independence and Validation

In order to verify the validity of the current model, it was necessary to test the grid sensitivity of the whole fluid region. In this work, three mesh cases were constructed, which were composed of 321,489, 928,746 and 3,356,160 elements, respectively. The grid sensitivity test was carried out with the aluminium foam 10 PPI and porosity of 0.918 at 7 gs^{-1} cooling air. The results are shown in Table 4, it can be seen that all the results were very close. Finally, mesh 2 was selected for this work.

Table 4. Grid independency tests.

Mesh No.	Mesh 1	Mesh 2	Mesh 3
No of element	321,489	928,746	3,356,160
T_{av} , °C	31.80	31.82	31.82
T_{max} , °C	33.32	33.32	33.35
T_{min} , °C	29.67	29.70	29.69
P_d , Pa	61.34	61.49	61.22

The numerical results were compared with Saw et al. [35], which are shown in Tables 5 and 6. Under the forced air-cooling condition without/with foam aluminium, the predicted numerical results agreed well with Saw's results, the maximum error between the present study and Saw was no more than 7%. Through these tests, the validity of the current model was verified.

Table 5. Comparison of battery temperature without AFHS [35].

Mass Flow Rate, gs^{-1}	10	20	40	60	80	100
Saw et al., °C	58.1	45.9	40.0	37.2	35.5	34.7
Present Study, °C	57.50	45.67	38.99	36.44	35.08	34.22
Error, %	1.04	0.50	2.53	2.05	1.19	1.39

Table 6. Comparison of battery temperature with AFHS [35].

Sample	Mass Flow Rate, gs^{-1}	10	15	20	25	30	35	40
10 PPI 0.682	Saw et al., °C	34.9	33.5	32.3	31.6	31.5	31.2	30.8
	Present Study, °C	35.39	33.83	33.07	32.61	32.3	32.07	31.9
	Error, %	1.4	0.99	2.38	3.2	2.54	2.8	3.58
20 PPI 0.774	Saw et al., °C	34.9	33.8	32.6	32.1	31.8	31.3	31.1
	Present Study, °C	35.66	34.1	33.3	32.89	32.56	32.33	32.15
	Error, %	2.17	0.89	2.27	2.44	2.4	3.29	3.37
40 PPI 0.923	Saw et al., °C	35.2	33.8	32.7	32.1	31.8	31.6	31.5
	Present Study, °C	37.07	35.55	34.78	34.27	33.88	33.57	33.32
	Error, %	5.33	5.18	6.37	6.76	6.55	6.25	5.78

4. Results and Discussion

An air-cooling BTMS has the advantages of light weight, low cost, convenient maintenance and no hidden danger of coolant leakage. The current research aimed to investigate the thermal performance of the forced air-cooling BTMS using AFHS, thus the maximum temperature of the battery, the temperature difference of the battery, and the pressure drop are the important factors that should be considered for the air-cooling BTMS. The flow and thermal performance of AFHS under different parameters were studied, and the results were compared with that without AFHS.

4.1. Air-Cooling BTMS without AFHS

Figure 3a shows the temperature distribution of the battery without AFHS at the mass flow rate $q_m = 10 \text{ gs}^{-1}$. It can be seen that the temperature downstream of the battery was

higher than that upstream along the air flow direction. The reason for this phenomenon is that when the air flows through the battery surface, the air first transfers heat with the upstream of the battery, resulting in the rapid reduction of the cooling capacity of the air and reduces the heat transfer performance downstream. Hence, the battery temperature is not evenly distributed. Figure 3b shows the pressure drop P_d between inlet and outlet without AFHS; it can be seen that the P_d increased gradually with the increase of mass flow rate q_m . The average temperature T_{av} and temperature difference T_d of the battery under different mass flow rates of cooling air are shown in Figure 3c,d, respectively. Obviously, there was a negative correlation between the T_{av} and the q_m . The T_{av} decreased with the increase of q_m . In order to keep the maximum temperature of the battery lower than 40 °C, at least 15 gs^{-1} of cooling air is required. Similarly, the temperature difference T_d also decreases with the increase of q_m , and the T_d is less than 3 °C at 15 gs^{-1} of cooling air.

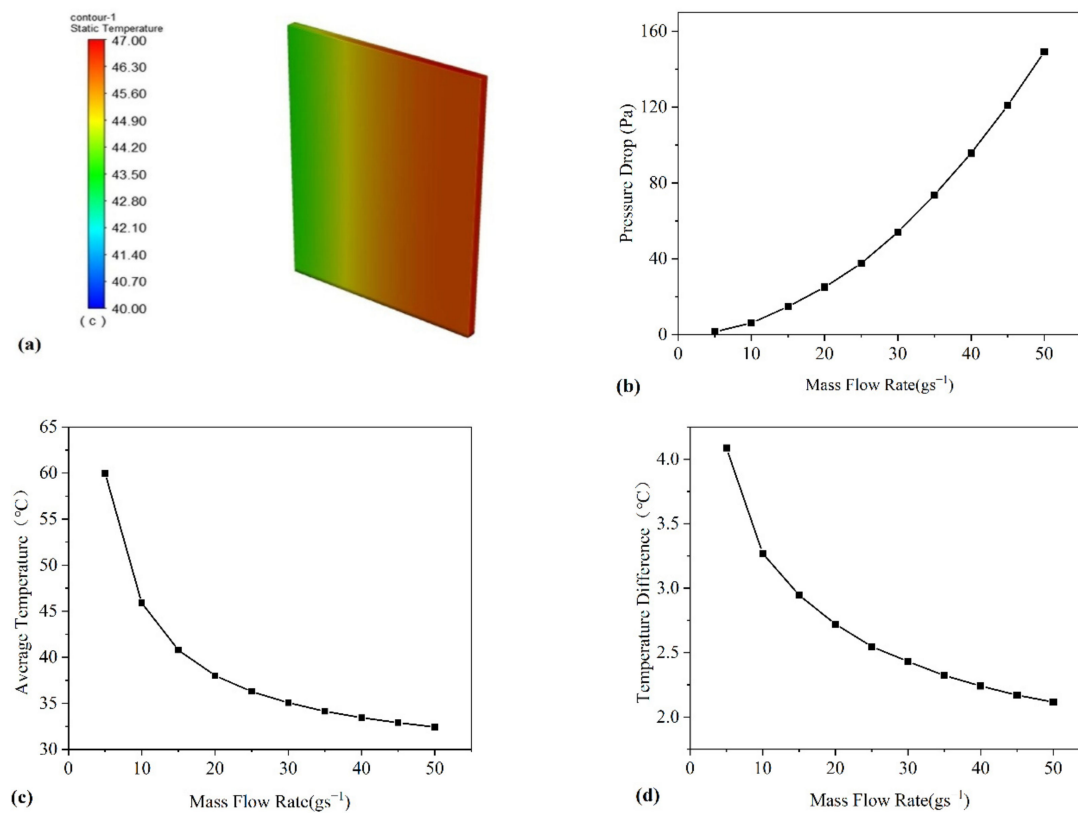


Figure 3. Air-cooling BTMS without AFHS: (a) temperature distribution of battery at $q_m = 10 \text{ gs}^{-1}$, (b) pressure drop, (c) average temperature, and (d) temperature difference.

4.2. Air-Cooling BTMS with Homogeneous AFHS

The open-cell aluminium foam has many irregularly shaped fluid channels; when cooling air flows through these channels, the heat transfers between the air and the three-dimensional network structure under the action of forced convection. On the one hand, the complex three-dimensional network structure of aluminium foam enhances the nonlinear effect of fluid. On the other hand, the large specific surface area of the aluminium foam is also an important reason for its good heat transfer performance. In addition, the high thermal conductivity of aluminium is also one of the factors to improve the heat transfer capacity. As a carrier of rapid heat transfer, the solid skeleton of the aluminium foam with high thermal conductivity is conducive to the uniform temperature of the whole porous area, transferring the heat to the fluid as soon as possible and accelerating the heat transfer process.

Figure 4 shows the pressure drop P_d versus mass flow rate q_m with different parameters of AFHS. In all cases, the increase of q_m led to the increase of P_d . In addition, at the same

pore density, the poor permeability of the aluminium foam with lower porosity resulted in a higher P_d . Moreover, pore density has a remarkable influence on P_d , the aluminium foam with large pore density has more ligaments, and the surface area of the solid aluminium skeleton per unit volume is much larger than that of low pore density foam, resulting in more flow resistance. Therefore, under the approximate porosity, the 40 PPI aluminium foam produced a higher P_d than 10 and 20 PPI aluminium foam.

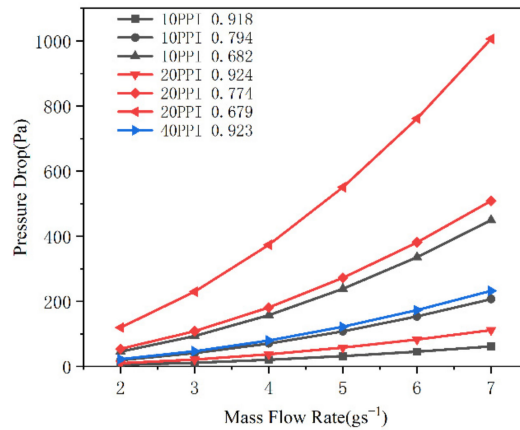


Figure 4. Pressure drop versus mass flow rate with different parameters of AFHS.

Figure 5a,b show the temperature distribution of the battery at 5 gs⁻¹ of cooling air for 10 PPI AFHS with a porosity of 0.918 and 0.682, respectively. It can be seen that the temperature distribution trend was similar to the case that without using AFHS, the temperature of the battery gradually increased along the direction of air flow. However, the T_{av} of the battery was significantly lower than the case without AFHS.

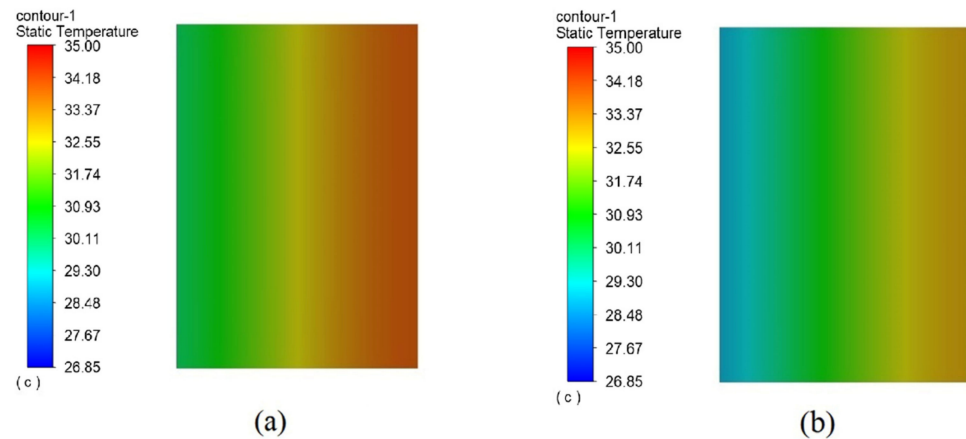


Figure 5. Temperature distributions of battery: (a) 10 PPI aluminium foam with 0.918 porosity, (b) 10 PPI aluminium foam with 0.682 porosity.

Figure 6 shows the average temperature T_{av} of the battery with different parameters of AFHS. At 5 gs⁻¹ of cooling air, the T_{av} of the battery with AFHS was below 34 °C, the temperature control ability was much better than that without AFHS. It can also be seen that at a constant mass flow rate q_m and PPI, the battery with large porosity of AFHS had a higher T_{av} . That is because there are more pores in large porosity AFHS, so the effective convective heat transfer area per unit volume is smaller. In contrast, the effective convective heat transfer area per unit volume of low porosity AFHS was larger, and a better cooling effect was achieved in air forced convection. As a result, the battery with low porosity AFHS had a lower T_{av} . When the AFHS had a similar porosity, the effect of PPI on the T_{av} was negligible at a constant q_m . For example, when the q_m was 2 gs⁻¹, the T_{av} of the battery

with 10 PPI and 0.918 porosity AFHS was 39.92 °C, while the T_{av} of battery with 20 PPI and 0.924 porosity AFHS was 39.87 °C.

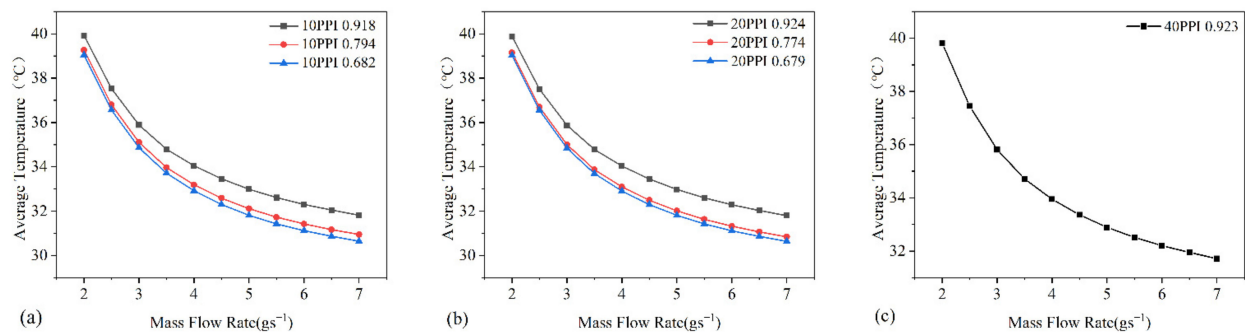


Figure 6. The average temperature of the battery with different parameters of AFHS: (a) 10 PPI aluminium foam; (b) 20 PPI aluminium foam; (c) 40 PPI aluminium foam.

When the cooling air flows over the surface of the battery, it first takes away the heat upstream, so the cooling capacity decreases gradually along the flow direction, resulting in the downstream temperature always being higher than the upstream temperature. This is the main reason for the uneven temperature of the battery. The T_d of the battery should be as small as possible to ensure safety and electrical performance. Figure 7 shows the T_d of the battery with different parameters of AFHS. It can be seen that the T_d of the battery with AFHS was negatively related to mass flow rate q_m , that is, the T_d decreased with the increase of q_m . It is worth noting that the T_d of the battery increased significantly with AFHS compared with that without AFHS. For LIB, the ideal T_d was less than 5 °C. However, the T_d of the battery was found to exceed 7 °C at $q_m = 2 \text{ gs}^{-1}$. In all cases, at least 5 gs^{-1} of cooling air is required to achieve T_d of below 5 °C.

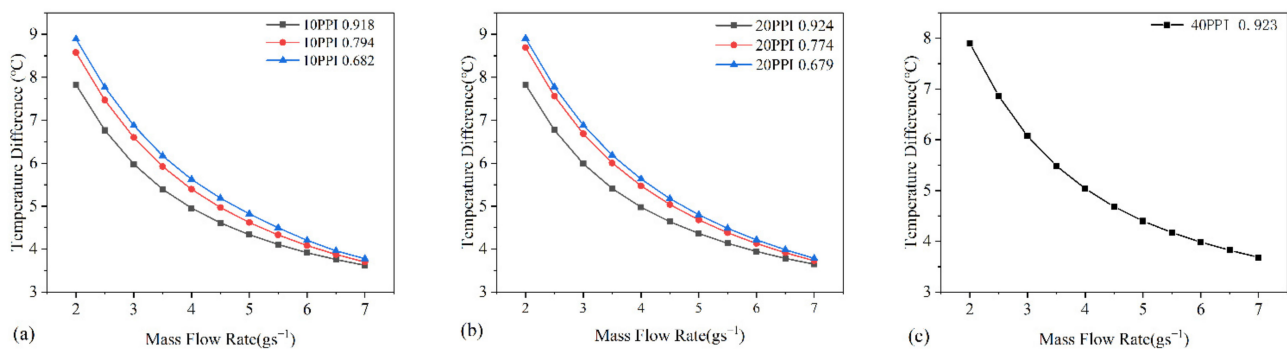


Figure 7. The temperature difference of the battery when using AFHS with different parameters: (a) 10 PPI aluminium foam; (b) 20 PPI aluminium foam; (c) 40 PPI aluminium foam.

When the mass flow rate q_m and pore density of AFHS remain unchanged, the temperature difference T_d of the battery is also negatively related to the porosity of the AFHS, that is, the larger the porosity, the smaller the T_d of the battery, while the pore density of AFHS has barely any effect on the T_d of the battery. For example, at $q_m = 5 \text{ gs}^{-1}$, the T_d of the battery is 4.39 °C when using AFHS with 10 PPI and 0.794 porosity, while the T_d of the battery with AFHS of 20 PPI and 0.774 porosity is 4.36 °C.

Figure 8a shows the relationship between the temperature control coefficient α and the pumping power Ω , the range of pumping power represents the power of the different systems maintaining the mass flow at 2 to 7 gs^{-1} . In all cases, the α increased with the increase of the Ω , but it rose more slowly at a high pumping power. In addition, the α of low porosity AFHS was slightly larger in the whole pumping power range, but more pumping power was needed to achieve the same α . Figure 8b shows variations in

temperature uniformity coefficient β with the pumping power Ω for various cases. Since the temperature difference was greater than 5°C at low mass flow, the β was less than 0 at low pumping power. In the whole pumping power range, the β of high porosity AFHS was higher than that of low porosity AFHS, and less pumping power was needed to reach the same β , which means that the battery temperature field uniformity with high porosity AFHS is better.

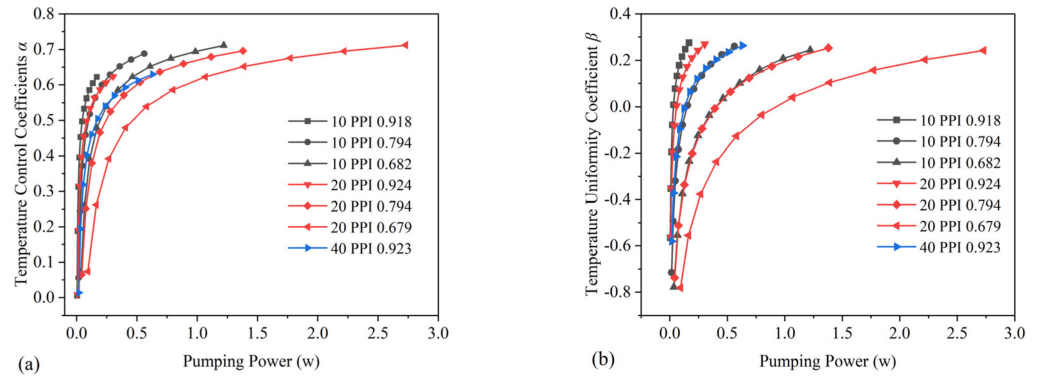


Figure 8. (a) Temperature control coefficient α , (b) temperature uniformity coefficient β .

Figure 9 shows the figure of merit (FOM) versus mass flow rate q_m when using the AFHS of different porosity and pore density. The results show that the FOM value was larger than 1 in all cases, which indicates the comprehensive convection performance of AFHS with different parameters was better than that without AFHS. When the pore density remained unchanged, the average surface heat transfer coefficient of the AFHS with larger porosity was smaller, while the accompanying pumping power was also smaller, which eventually led to a higher FOM. In addition, when the porosities were similar, the AFHS with larger PPI consumed more pumping power, resulting in a lower FOM. For all calculated parameters above 10 PPI and 0.918 porosity, AFHS had the highest FOM, indicating that it performed better than the others when considering heat convection and energy dissipation.

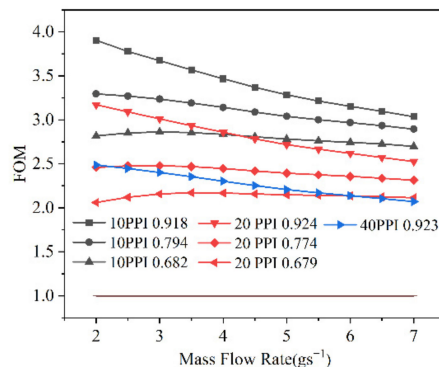


Figure 9. FOM versus mass flow rate.

4.3. Air-Cooling BTMS with the AFHS of Gradient Porosity Designs

Compared with the situation without AFHS, using homogeneous AFHS could remarkably enhance the thermal performance, but pressure drop and temperature differences were even greater. Therefore, the gradient design in aluminium foam was considered to reduce flow resistance and improve temperature uniformity. Considering that the pore density has little effect on the heat transfer characteristics, the gradient porosity designs were adopted in subsequent analyses, and the pore density was all 10 PPI.

The gradient of porosity is controlled by the following equation:

$$\begin{aligned} \varepsilon &= \varepsilon_{\min} + (\varepsilon_{\max} - \varepsilon_{\min})\left(\frac{x}{l}\right)^m \\ \varepsilon &= \varepsilon_{\max} - (\varepsilon_{\max} - \varepsilon_{\min})\left(\frac{x}{l}\right)^m \end{aligned} \tag{17}$$

where ε_{\max} and ε_{\min} are the maximum and minimum porosity, respectively, in the current study $\varepsilon_{\max} = 0.92$ and $\varepsilon_{\min} = 0.68$; m represents the parameter controlling the porosity; x/l is the normalised distance.

The variation of the porosity gradient of aluminium foam for increasing and decreasing patterns is shown in Figure 10. For the porosity-increasing gradient pattern (PIGP), $m = 0.1, 1, \text{ and } 10$ correspond to the equivalent homogeneous porosity levels of 0.9, 0.8 and 0.7, respectively, while for the porosity-decreasing gradient pattern (PDGP), $m = 0.1, 1, \text{ and } 10$ correspond to the equivalent homogeneous porosity levels of 0.7, 0.8 and 0.9, respectively.

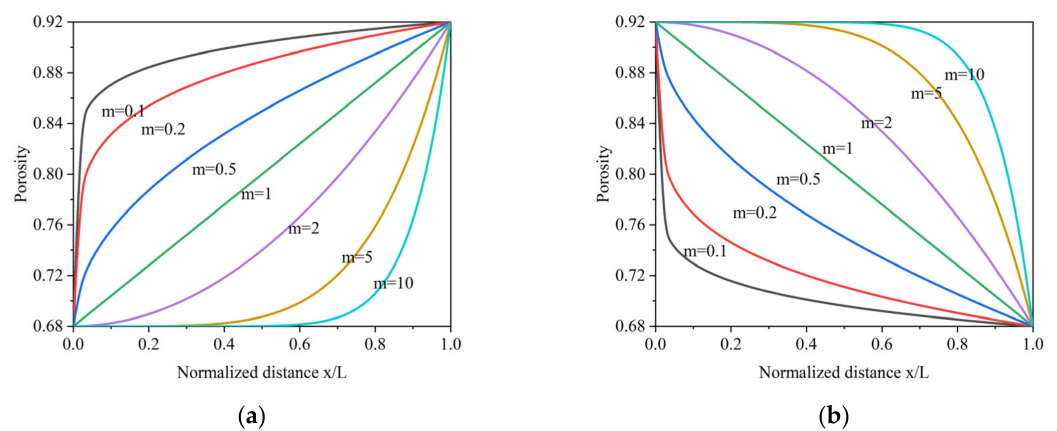


Figure 10. Variation of porosity gradient versus normalised distance: (a) porosity-increasing gradient pattern, (b) porosity-decreasing gradient pattern.

The gradient porosity can be realised by the user-defined function UDF in Ansys-fluent, and the change of coefficient of viscous resistance terms and inertial resistance terms caused by the change of gradient porosity can be calculated by the Ergun formula [37]. The porosity is set to change perpendicular to the flow direction (Z-axis direction) and along the flow direction (X-axis direction), and C_1 and C_2 change accordingly with porosity.

4.3.1. AFHS of Gradient Porosity Designs in the Z-Axis Direction (Perpendicular to the Flow Direction)

Figure 11 shows the pressure drop P_d of AFHS with gradient porosity designs in the Z-axis direction (perpendicular to the flow direction). As can be seen, there was no difference in P_d between using PIDP and PDGP at the same equivalent porosity, indicating that the two patterns have the same influence on flow performance in the Z-axis direction. Moreover, the P_d of the two patterns was lower than that of the homogeneous porosity AFHS at the same equivalent porosity, which indicates that the gradient porosity designs in the Z-axis direction can improve the flow performance. The reason for this phenomenon is that when the porosity change direction is perpendicular to the flow direction, the air tends to flow to the part with large porosity at a higher speed, so the overall flow resistance decreases and the pressure drop decreases.

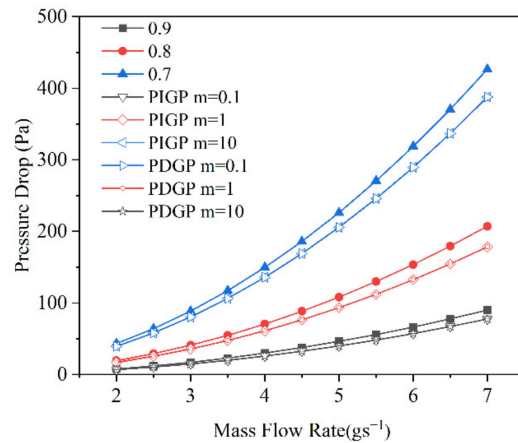


Figure 11. Pressure drop with AFHS of gradient porosity designs in the Z-axis direction.

Figure 12 shows the battery temperature distributions with AFHS in the two gradient patterns at $q_m = 5 \text{ gs}^{-1}$, but the difference between the two cases is not obvious. Figure 13a shows the average temperature T_{av} of the battery with the AFHS of gradient porosity designs in the Z-axis direction. We can see that the T_{av} of the battery with AFHS of PIGP was almost the same as that with equivalent homogeneous porosity AFHS, while the T_{av} of the battery with AFHS of PDGP was higher than that with equivalent homogeneous porosity AFHS. This is mainly because the porosity near the heating surface is large with the PDGP, and the solid skeleton volume in the porous medium area is small, which makes the heat conduction between the aluminium foam and the heated surface deteriorate, and ultimately leads to a weakening in the heat transfer effect. Figure 13b shows the T_d of the battery with the AFHS with gradient porosity designed in the Z-axis direction. The T_d of the battery with AFHS of PIGP was almost the same as that with the equivalent homogeneous porosity AFHS. However, using the AFHS of PDGP leads to T_d being slightly less than that at the equivalent porosity.

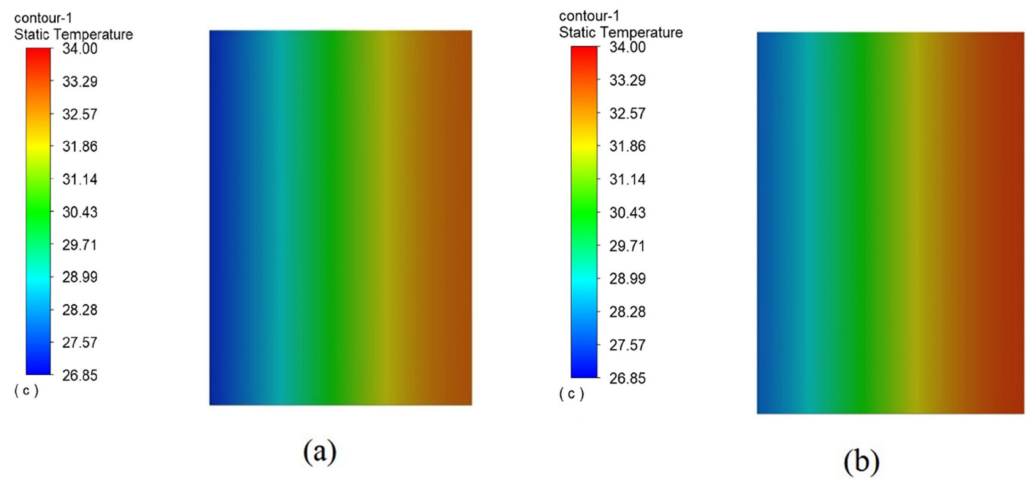


Figure 12. Temperature distributions of battery: (a) using AFHS with porosity-increasing gradient pattern $m = 1$, (b) using AFHS with porosity-decreasing gradient pattern $m = 1$.

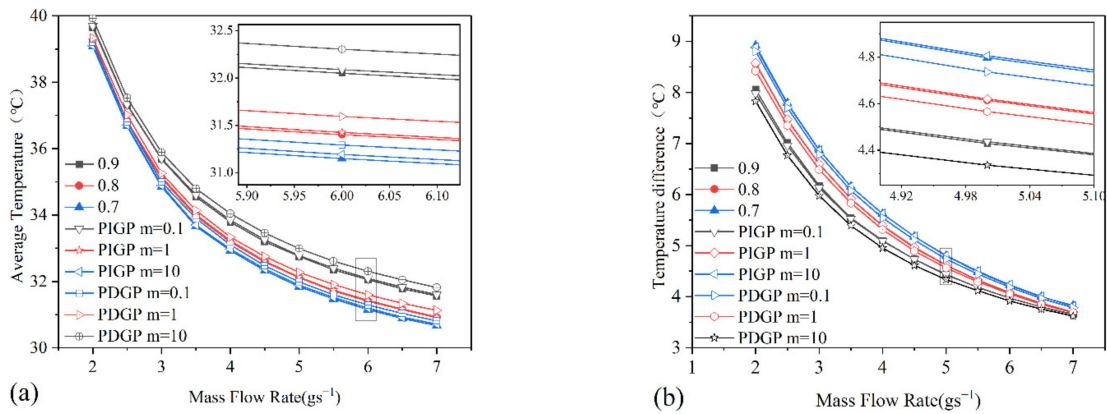


Figure 13. (a) Average temperature of battery, (b) temperature difference of battery (with AFHS with gradient porosity designed in the Z-axis direction).

Figure 14a shows the temperature control coefficient α versus pumping power Ω with AFHS with gradient porosity designed in the Z-axis direction. At low porosity level, the α was slightly greater over the entire pumping power range. Within a constant porosity level, there was no obvious difference in the α . However, it can be seen from the enlarged figure, when the α with the homogeneous porosity AFHS was equal to that with AFHS of PIGP, the Ω required for AFHS of PIGP was smaller. When the same Ω was required for AFHS of PIGP and PDGP, the AFHS of PIGP had a lower T_{av} , resulting in the AFHS of PIGP having a larger α than that of PDGP. At low pumping power ($\Omega < 0.2$ W), the AFHS of PIGP with $m = 0.1$ had the highest α . Figure 14b shows the temperature uniformity coefficient β versus pumping power Ω with the AFHS with gradient porosity designed in the Z-axis direction. As the mass flow rate increased, the T_d of the battery with AFHS of different gradients became closer, so the maximum value of β was almost the same in the whole pumping power range. Since the T_d of the battery with AFHS of PDGP was smaller than that of PIGP under the same equivalent porosity level, it led to a slightly larger β with PDGP.

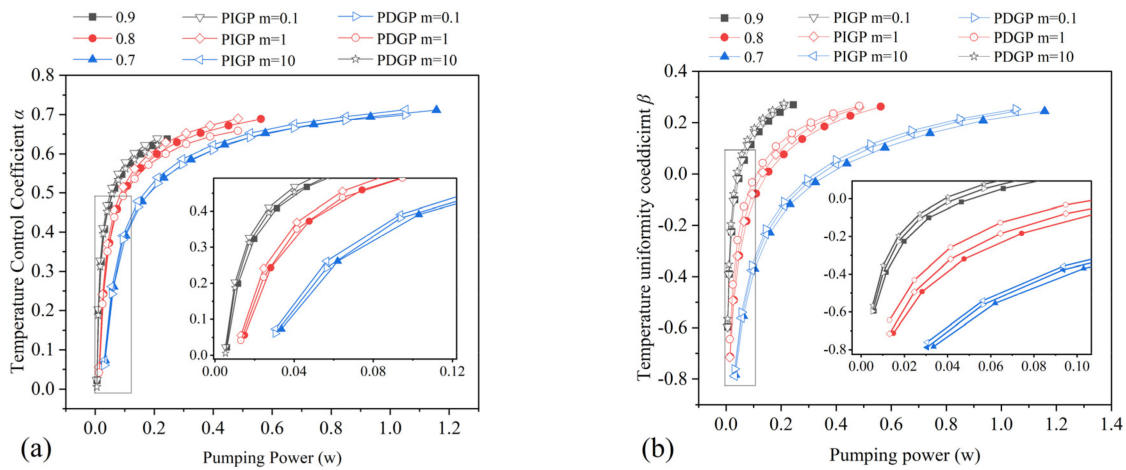


Figure 14. (a) Temperature control coefficient α , (b) temperature uniformity coefficient β (with AFHS with gradient porosity designed in the Z-axis direction).

Figure 15 shows FOM versus mass flow rate with the AFHS with gradient porosity designed in the Z-axis direction. Compared with the homogeneous porosity AFHS, the AFHS with gradient porosity designed in the Z-axis direction (perpendicular to the flow direction) reduces the pressure drop. Therefore, with little difference in heat transfer performance, the AFHS of PIGP required less pumping power and resulted in a larger FOM. Meanwhile, the AFHS of PDGP had a small convective heat transfer coefficient

leading to a smaller FOM. Considering the heat convection and energy consumption, an AFHS with PIGP in the Z-axis direction is superior to those with homogeneous porosity.

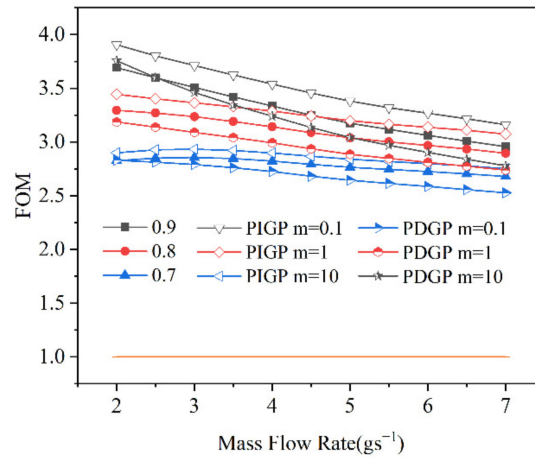


Figure 15. FOM versus mass flow rate (with AFHS with gradient porosity designed in the Z-axis direction).

4.3.2. AFHS with Gradient Porosity Designed in the X-Axis Direction (the Flow Direction)

Figure 16 shows the pressure drop P_d of AFHS with gradient porosity designed in the X-axis direction (the air flow direction). At the same porosity levels, the pressure drop of AFHS with gradient porosity designed in the X-axis direction was not significantly different from that of homogeneous porosity AFHS. This means that the gradient porosity designed in the X-axis direction will not improve the flow performance of the AFHS.

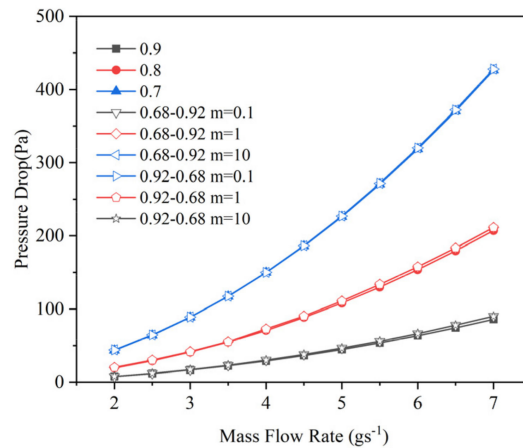


Figure 16. Pressure drop with AFHS with gradient porosity designed in the X-axis direction.

Figure 17a,b shows temperature distributions of battery with AFHS with gradient porosity designed in the X-axis direction. Figure 17c shows the T_{av} of the battery with AFHS with gradient porosity designed in the X-axis direction. It was found that at the same porosity level, whether using the AFHS of PIGP or PDGP, the T_{av} was almost unchanged, which was slightly higher than that with the equivalent homogeneous porosity AFHS, indicating the gradient porosity designed in the X-axis direction has no effect on reducing the T_{av} .

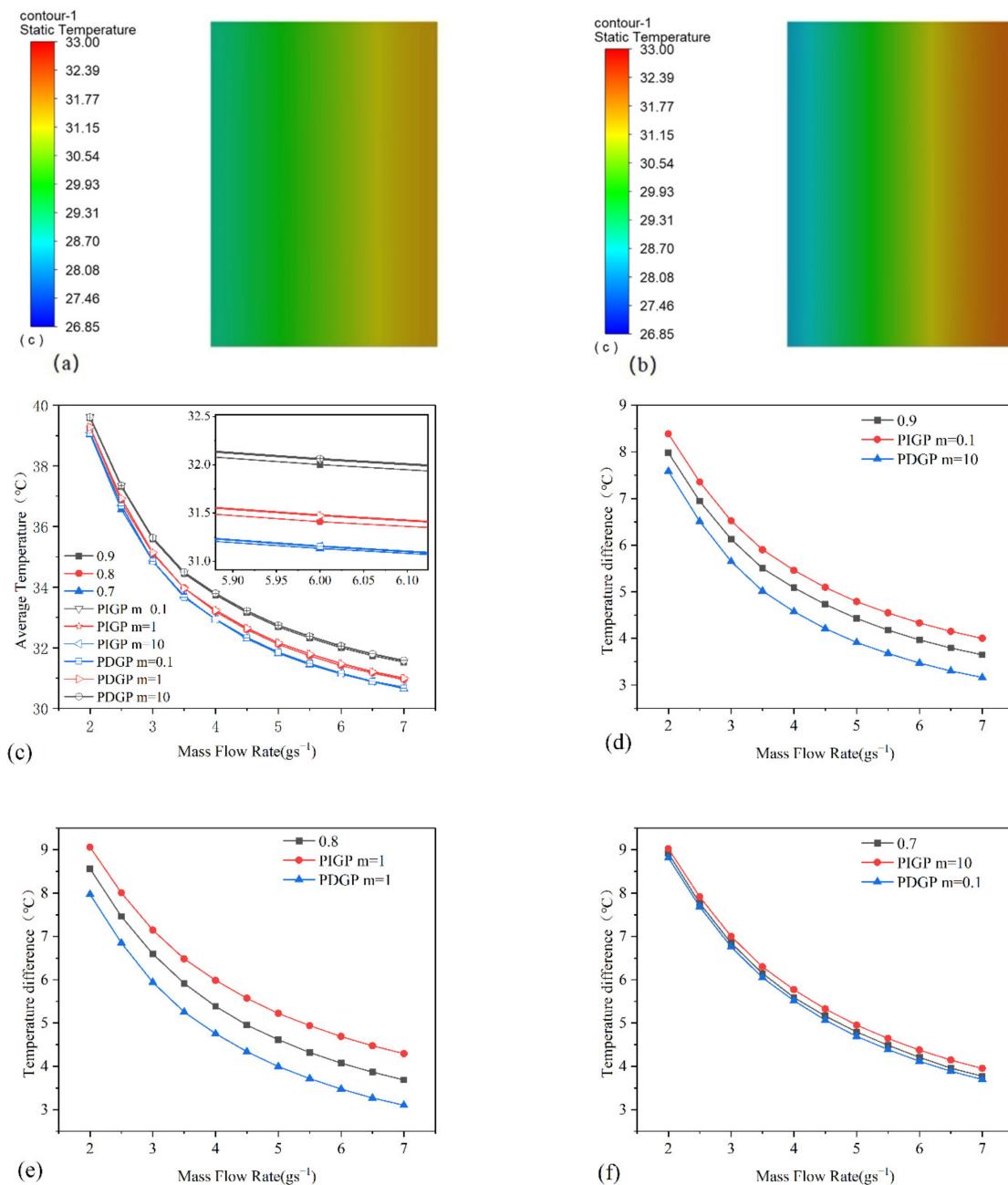


Figure 17. With AFHS with gradient porosity designed in the X-axis direction: (a) temperature distributions of battery with AFHS of PDGP m = 1; (b) temperature distributions of battery with AFHS of PIGP m = 1; (c) average surface temperature; (d) temperature difference of equivalent porosity = 0.9, (e) temperature difference of equivalent porosity = 0.8, and (f) temperature difference of equivalent porosity = 0.7.

To show the influence of gradient porosity designed along the flow direction on temperature difference T_d more directly, the T_d of the battery was divided into three figures according to the equivalent porosity level, which are shown in Figure 17d–f. Under the same porosity level, the battery with AFHS of PDGP had a smaller temperature difference, while with AFHS of PIGP had a larger temperature difference compared with the equivalent homogeneous porosity AFHS. During the cooling process, the cooling air shows the trend of increasing its temperature, which results in the upstream of the battery along the flow direction generally having a better cooling effect than the downstream. Therefore, the idea of reducing the battery temperature difference is to weaken the upstream heat transfer

effect or strengthen the downstream heat transfer effect. Compared with the homogeneous porosity AFHS, when the porosity decreases along the flow direction, the upstream high porosity aluminum foam has more internal pores, and the effective heat transfer area per unit volume is smaller, thus weakening the heat transfer effect of the upstream of the battery. The low-porosity aluminum foam in the downstream has a larger effective heat transfer area, which strengthens the downstream heat transfer effect, so the temperature difference decreases. As the porosity increases along the flow direction, the upstream low-porosity aluminum foam has more convective heat transfer area, thereby enhancing the heat transfer effect in the upstream of the battery, while the downstream high porosity aluminium foam weakens the heat transfer effect, thus resulting in the increase of the temperature difference. Comparing the above three figures, it can also be found that using the AFHS of PDGP with $m = 1$, the lowest temperature difference was $T_d = 3.1\text{ }^\circ\text{C}$ at $q_m = 7\text{ gs}^{-1}$.

Figure 18a shows temperature control coefficient α with AFHS with gradient porosity designed in the Z-axis direction. Since the average temperature of battery and pressure drop under the same porosity level were almost identical, the temperature control coefficients α were basically the same. The temperature uniformity coefficient β with AFHS with gradient porosity designed in the Z-axis direction is shown in Figure 18b. Obviously, using the AFHS of PDGP can significantly improve the β under the same equivalent porosity level. Meanwhile, when using AFHS with PDGP in the x -axis direction, the β with $m = 10$ was similar to that of $m = 0.1$, but less pumping power was required with $m = 10$. Thus, the AFHS of PDGP with $m = 10$ is a better design to reduce the battery temperature difference.

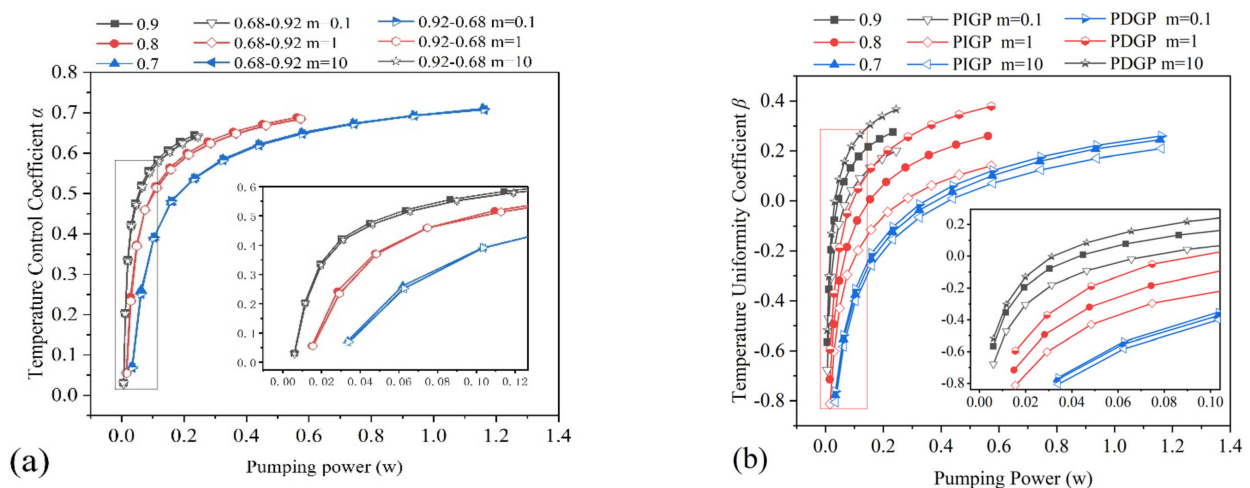


Figure 18. (a) Temperature control coefficient α , (b) temperature uniformity coefficient β (with AFHS with gradient porosity designed in the X-axis direction).

Figure 19 shows the FOM with AFHS with gradient porosity designed in the X-axis direction. According to the above analysis, compared with the homogeneous porosity AFHS, the AFHS of PIGP in the X-axis direction strengthened the heat transfer effect, while the PDGP in the X-axis direction weakened the heat transfer effect. Since the pumping power was the same, the FOM of PIGP was greater than that of PDGP. Although AFHS of PIGP with $m = 0.1$ in the X-axis direction had the largest FOM, the battery with that had the worst temperature uniformity.

To sum up, the use of AFHS in BTMS will significantly enhance the thermal performance, but it will also increase the flow resistance and pressure drop, resulting in additional energy loss. However, Giuliano et al. [33] indicated that the parasitic power consumption of a battery pack with liquid cooling was 1200 w–2000 w, while the pump power of a uniform foam aluminium heat sink with 20 ppi was 730 w–1500 w. Thus, the use of foam aluminium heat sink is acceptable. The AFHS of gradient porosity design further reduce the pressure drop and battery temperature difference. In the process of practical application,

comprehensive optimisation can be carried out according to specific conditions to achieve the best cooling effect.

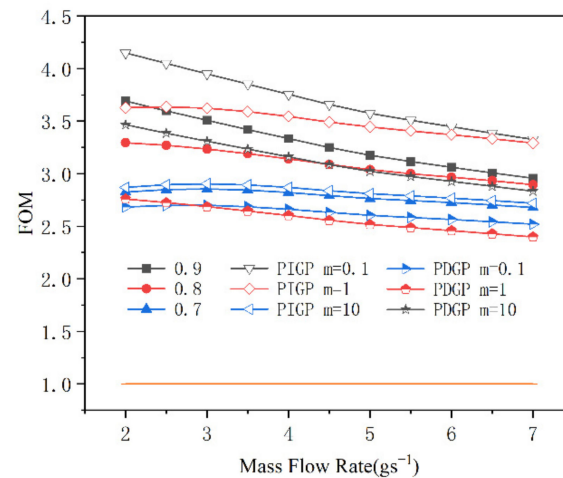


Figure 19. FOM with AFHS with gradient porosity designed in the X-axis direction.

5. Conclusions

Three-dimensional computational fluid dynamic analysis was carried out to investigate an air-cooling Li-ion battery module with the aluminium foam heat sink (AFHS). The effects of porosity and pore density of homogeneous AFHS on the thermal management performance of the battery module were investigated from the aspects of pressure drop P_d , battery average temperature T_{av} and temperature difference T_d . Furthermore, four types of gradient porosity designs with the different porosity controlling parameter m were tested and compared. The results led to the following conclusions:

Compared with not using AFHS, the use of AFHS significantly reduces the average temperature of the battery, but also brings the consequence of the increase of the pressure drop and temperature difference. The decrease of the porosity of AFHS reduces the battery average temperature, but increases the temperature difference. Increasing the pore density of the AFHS will lead to increases in pressure drop, but has little effect on thermal performance.

The gradient porosity designed in the direction perpendicular to the flow can improve flow performance, and reduce the pressure drop. Although the thermal performance of the battery module with the AFHS of porosity-increasing gradient pattern (PIGP) is better than that with the AFHS of porosity-decreasing gradient pattern (PDGP), neither of the two types of gradient porosity designs reduces the average temperature of the battery compared to the homogeneous porosity AFHS. Considering the energy consumption and thermal performance, the porosity-increasing pattern with $m = 0.1$ is the best design among the six configuration designs.

The gradient porosity designs in the flow direction have no obvious effect on the pressure drop. However, under the same porosity level, compared with homogeneous porosity AFHS, the AFHS of PDGP reduces the battery temperature difference, while the AFHS of PIGP increases the battery temperature difference. Using the AFHS of PDGP $m = 1$, the minimum temperature difference $T_d = 3.10$ °C is obtained at $q_m = 7$ gs⁻¹, which is 16.2% lower than that of AFHS of homogeneous porosity.

Author Contributions: Conceptualisation, P.W. and D.Q.; formal analysis, T.W.; methodology, P.W.; project administration, D.Q. and T.W.; supervision, D.Q.; validation, J.C.; writing—original draft, P.W.; writing—review and editing, P.W. and J.C. All authors have read and agreed to the published version of the manuscript.

Funding: This work was supported by the National Key R&D Program “New energy vehicles” of China (Project No.2018YFB0106204).

Institutional Review Board Statement: Not applicable.

Informed Consent Statement: Not applicable.

Data Availability Statement: Data is contained within the article.

Conflicts of Interest: The authors declare that they have no known competing financial interests or personal relationships that could have appeared to influence the work reported in this paper.

Nomenclature

q	heating rate per unit volume of the battery, $W m^{-3}$
V	volume of the battery, m^3
U_o	open circuit potential of the battery, V
U	battery voltage, V
T	battery temperature, $^{\circ}C$
ρ_b	density of the battery, $kg m^{-3}$
C_{pb}	heat capacity of the battery, $J kg^{-1}K^{-1}$
k_b	thermal conductivity of the battery, $W m^{-1}k^{-1}$
ρ_f	density of fluid, $kg m^{-3}$
v	average speed vector, $m s^{-1}$
p	static pressure, pa
s	source term
C_1	viscous resistance, m^{-2}
C_2	the internal resistance, m^{-1}
k_f	thermal conductivity of fluid, $W m^{-1}k^{-1}$
k_s	thermal conductivity of solid, $W m^{-1}k^{-1}$
k_{eff}	effective thermal conductivity, $W m^{-1}k^{-1}$
ε	porosity
d_p	pore size, mm
PPI	number of pores per inch
Nu	Nusselt number
H	average convective heat transfer coefficient
A_{con}	base area of the heat sink
T_{in}	inlet air temperature
T_w	average temperature of heat transfer wall
D	equivalent diameter of heat sink, m
T_{av}	average temperature of battery, $^{\circ}C$
T_d	temperature difference of battery, $^{\circ}C$
α	temperature control coefficient
β	temperature uniformity coefficient
FOM	figure of merit
Ω	pumping power, W

References

1. Requia, W.J.; Mohamed, M.; Higgins, C.D.; Arain, A.; Ferguson, M. How clean are electric vehicles? Evidence-based review of the effects of electric mobility on air pollutants, greenhouse gas emissions and human health. *Atmos. Environ.* **2018**, *185*, 64–77. [[CrossRef](#)]
2. Ke, W.; Zhang, S.; He, X.; Wu, Y.; Hao, J. Well-to-wheels energy consumption and emissions of electric vehicles: Mid-term implications from real-world features and air pollution control progress. *Appl. Energ.* **2017**, *188*, 367–377. [[CrossRef](#)]
3. Bahiraei, F.; Fartaj, A.; Nazri, G.A. Electrochemical-thermal modeling to evaluate active thermal management of a lithium-ion battery module. *Electrochim. Acta* **2017**, *254*, 59–74. [[CrossRef](#)]
4. Ramadass, P.; Haran, B.; White, R.; Popov, B.N. Capacity fade of Sony 18650 cells cycled at elevated temperatures: Part I. Cycling performance. *J. Power Sources* **2002**, *112*, 606–613. [[CrossRef](#)]
5. Ramadass, P.; Haran, B.; White, R.; Popov, B.N. Capacity fade of Sony 18650 cells cycled at elevated temperatures: Part II. Capacity fade analysis. *J. Power Sources* **2002**, *112*, 614–620. [[CrossRef](#)]
6. Belt, J.; Utgikar, V.; Bloom, I. Calendar and PHEV cycle life aging of high-energy, lithium-ion cells containing blended spinel and layered-oxide cathodes. *J. Power Sources* **2011**, *196*, 10213–10221. [[CrossRef](#)]

7. Wang, Q.; Ping, P.; Zhao, X.; Chu, G.; Sun, J.; Chen, C. Thermal runaway caused fire and explosion of lithium ion battery. *J. Power Sources* **2012**, *208*, 210–224. [[CrossRef](#)]
8. Duh, Y.S.; Theng, J.H.; Chen, C.C.; Kao, C.S. Comparative study on thermal runaway of commercial 14500, 18650 and 26650 LiFePO₄ batteries used in electric vehicles. *J. Energy Storage* **2020**, *31*, 101580. [[CrossRef](#)]
9. Wang, Y.; Gao, Q.; Wang, G.; Lu, P.; Zhao, M.; Bao, W. A review on research status and key technologies of battery thermal management and its enhanced safety. *Int. J. Energy Res.* **2018**, *42*, 4008–4033. [[CrossRef](#)]
10. Arora, S.; Shen, W.; Kapoor, A. Review of mechanical design and strategic placement technique of a robust battery pack for electric vehicles. *Renew. Sustain. Energy Rev.* **2016**, *60*, 1319–1331. [[CrossRef](#)]
11. Lamb, J.; Orendorff, C.J.; Steele, L.A.M.; Spangler, S.W. Failure propagation in multi-cell lithium ion batteries. *J. Power Sources* **2015**, *283*, 517–523. [[CrossRef](#)]
12. Väyrynen, A.; Salminen, J. Lithium ion battery production. *Chem. Thermodyn.* **2012**, *46*, 80–85. [[CrossRef](#)]
13. Thakur, A.K.; Prabakaran, R.; Elkadeem, M.R.; Sharshir, S.W.; Arıcı, M.; Wang, C.; Zhao, W.; Hwang, J.Y.; Saidur, R. A state of art review and future viewpoint on advance cooling techniques for Lithium-ion battery system of electric vehicles. *J. Energy Storage* **2020**, *32*, 101771. [[CrossRef](#)]
14. Kim, J.; Oh, J.; Lee, H. Review on battery thermal management system for electric vehicles. *Appl. Therm. Eng.* **2019**, *149*, 192–212. [[CrossRef](#)]
15. Patil, M.S.; Seo, J.H.; Panchal, S.; Jee, S.W.; Lee, M.Y. Investigation on thermal performance of water-cooled Li-ion pouch cell and pack at high discharge rate with U-turn type microchannel cold plate. *Int. J. Heat Mass Transf.* **2020**, *155*, 119728. [[CrossRef](#)]
16. Deng, Y.; Feng, C.; Jiaqiang, E.; Zhu, H.; Chen, J.; Wen, M.; Yin, H. Effects of different coolants and cooling strategies on the cooling performance of the power lithium ion battery system: A review. *Appl. Therm. Eng.* **2018**, *142*, 10–29. [[CrossRef](#)]
17. Verma, A.; Shashidhara, S.; Rakshit, D. A comparative study on battery thermal management using phase change material (PCM). *Therm. Sci. Eng. Prog.* **2019**, *11*, 74–83. [[CrossRef](#)]
18. Ping, P.; Peng, R.; Kong, D.; Chen, G.; Wen, J. Investigation on thermal management performance of PCM-fin structure for Li-ion battery module in high-temperature environment. *Energy Convers. Manage.* **2018**, *176*, 131–146. [[CrossRef](#)]
19. Jiang, K.; Liao, G.L.; Jiaqiang, E.; Zhang, F.; Chen, J.W.; Leng, E.W. Thermal management technology of power lithium-ion batteries based on the phase transition of materials: A review. *J. Energy Storage* **2020**, *32*, 101816. [[CrossRef](#)]
20. Ye, X.; Zhao, Y.; Quan, Z. Experimental study on heat dissipation for lithium-ion battery based on micro heat pipe array (MHPA). *Appl. Therm. Eng.* **2018**, *130*, 74–82. [[CrossRef](#)]
21. Jouhara, H.; Serey, N.; Khordehgah, N.; Bennett, R.; Almahmoud, S.; Lester, S.P. Investigation, development and experimental analyses of a heat pipe based battery thermal management system. *Int. J. Thermofluids* **2020**, *1–2*, 100004. [[CrossRef](#)]
22. Gan, Y.; He, L.; Liang, J.; Tan, M.; Xiong, T.; Li, Y. A numerical study on the performance of a thermal management system for a battery pack with cylindrical cells based on heat pipes. *Appl. Therm. Eng.* **2020**, *179*, 115740. [[CrossRef](#)]
23. Tran, T.H.; Harmand, S.; Desmet, B.; Filangi, S. Experimental investigation on the feasibility of heat pipe cooling for HEV/EV lithium-ion battery. *Appl. Therm. Eng.* **2014**, *63*, 551–558. [[CrossRef](#)]
24. Lyu, Y.; Siddique, A.R.M.; Majid, S.H.; Biglarbegian, M.; Gadsden, S.A.; Mahmud, S. Electric vehicle battery thermal management system with thermoelectric cooling. *Energy Rep.* **2019**, *5*, 822–827. [[CrossRef](#)]
25. Chen, K.; Wu, W.; Yuan, F.; Chen, L.; Wang, S. Cooling efficiency improvement of air-cooled battery thermal management system through designing the flow pattern. *Energy* **2019**, *167*, 781–790. [[CrossRef](#)]
26. Luo, W.; He, F.Q.; Huang, Q.; Li, X.X.; Zhong, Z. Experimental investigation on thermal performance of silica cooling plate-aluminate thermal plate-coupled forced convection-based pouch battery thermal management system. *Int. J. Energy Res.* **2019**, *43*, 7604–7613. [[CrossRef](#)]
27. Zhang, X.; Wang, R.; Li, X.G.; Lu, C.Y.; Wang, Z.K.; Wang, W.L. Energy Absorption Performance of Open-Cell Aluminum Foam and Its Application in Landing Buffer System. *J. Mater. Eng. Perform.* **2021**, *30*, 6132–6145. [[CrossRef](#)]
28. Kim, J.H.; Kim, d.; Lee, M.G.; Lee, J.K. Multiscale Analysis of Open-Cell Aluminum Foam for Impact Energy Absorption. *J. Mater. Eng. Perform.* **2016**, *25*, 3977–3984. [[CrossRef](#)]
29. Zhang, W.; Bai, X.; Bao, M. Heat transfer performance evaluation based on local thermal non-equilibrium for air forced convection in channels filled with metal foam and spherical particles. *Therm. Eng.* **2018**, *145*, 735–742. [[CrossRef](#)]
30. Zhang, Y.; Huang, J.; Cao, M.; Du, G.; Wang, L. A novel sandwich structured phase change material with well impact energy absorption performance for Li-ion battery application. *J. Energy Storage* **2021**, *40*, 102769. [[CrossRef](#)]
31. Mallow, A.; Abdelaziz, O.; Graham, S. Thermal charging performance of enhanced phase change material composites for thermal battery design. *Int. J. Ther. Sci.* **2018**, *127*, 19–28. [[CrossRef](#)]
32. Elidi, M.M.; Karkri, M.; Abdoutankari, M. A passive thermal management system of Li-ion batteries using PCM composites: Experimental and numerical investigations. *Int. J. Heat Mass Transf.* **2021**, *169*, 120894. [[CrossRef](#)]
33. Giuliano, M.R.; Prasad, A.K.; Advani, S.G. Experimental study of an air-cooled thermal management system for high capacity lithium-titanate batteries. *Power Sources* **2012**, *216*, 345–352. [[CrossRef](#)]
34. Mohammadian, S.K.; Zhang, Y. Cumulative effects of using pin fin heat sink and porous metal foam on thermal management of lithium-ion batteries. *Appl. Therm. Eng.* **2017**, *118*, 375–384. [[CrossRef](#)]
35. Saw, L.H.; Ye, Y.; Yew, M.C. Computational fluid dynamics simulation on open-cell aluminium foams for Li-ion battery cooling system. *Appl. Energy* **2017**, *204*, 1489–1499. [[CrossRef](#)]

36. Wang, Y.L.; Yu, Y.; Jing, Z.Q.; Wang, C.Y.; Zhou, G.; Zhao, W.Z. Thermal performance of lithium-ion batteries applying forced air cooling with an improved aluminium foam heat sink design. *Int. J. Heat Mass Transf.* **2021**, *167*, 120827. [[CrossRef](#)]
37. Hung, T.C.; Huang, Y.X.; Yan, W.M. Thermal performance analysis of porous-microchannel heat sinks with different configuration designs. *Int. J. Heat Mass Transf.* **2013**, *66*, 235–243. [[CrossRef](#)]
38. Ansys Inc. *Ansys-Fluent Theory Guide 19.0*; Ansys Inc.: Canonsburg, PA, USA, 2019.